Investigating the effects of a penetrating vessel occlusion with a multi-scale microvasculature model of the human cerebral cortex

Wahbi K. El-Bouri, Stephen J. Payne

Institute of Biomedical Engineering, Department of Engineering Science, University of Oxford, Parks Road, Oxford, OX1 3PJ, UK

Corresponding Address: Wahbi K. El-Bouri, Institute of Biomedical Engineering, Department of Engineering Science, University of Oxford, Parks Road, Oxford, OX1 3PJ, UK

+44 (0)1865 617696 wahbi.el-bouri@eng.ox.ac.uk

0. Abstract and Keywords

The effect of the microvasculature on observed clinical parameters, such as cerebral blood flow, is poorly understood. This is partly due to the gap between the vessels that can be individually imaged in humans and the microvasculature, meaning that mathematical models are required to understand the role of the microvasculature. As a result, a multi-scale model based on morphological data was developed here that is able to model large regions of the human microvasculature. From this model, a clear layering of flow (and 1-dimensional depth profiles) was observed within a voxel, with the flow in the microvasculature being driven predominantly by the geometry of the penetrating vessels. It also appears that the pressure and flow are decoupled, both in healthy vasculatures and in those where occlusions have occurred, again due to the topology of the penetrating vessels shunting flow between them. Occlusion of a penetrating arteriole resulted in a very high degree of overlap of blood pressure drop with experimentally observed cell death. However, drops in blood flow were far more widespread, providing additional support for the theory that pericyte controlled regulation on the capillary scale likely plays a large part in the perfusion of tissue post-occlusion.

Keywords: Cerebral microcirculation, micro-infarct, haemodynamics, cerebral blood flow, penetrating arterioles

1. Introduction

The microvasculature is recognized as playing a key role in both perfusion and oxygen transport in the brain. Any reduction of blood flow to the brain can lead to tissue death at a time scale of the order of tens of seconds to minutes. Increasingly, the microvasculature, and changes to its topology, has been linked to diseases such as Alzheimer's disease, vascular dementia, and brain tumours[1–4]. For example, although Alzheimer's disease, the leading cause of dementia, has traditionally been thought to be due to the formation of amyloid plaques and neurofibrillary tangles, it is now appreciated that there is also a strong vascular component to this pathology[5].

Despite the importance of the microvasculature in maintaining a healthy supply of blood and oxygen to the brain, little is known about the specific effects that the topology of these vessels has on blood and oxygen transport. This is predominantly due to the relatively low resolution of modern clinical imaging techniques that can only discern vessels larger than approximately 0.8 – 0.9 mm in diameter[6]. There is thus an imaging gap relating to the microvasculature of the human brain, which can only currently be filled using mathematical models. These models must be based on accurate physiological data, either obtained post-mortem or from animal models. To quantify this link between the microvasculature and clinical imaging techniques, models of the scale of a standard clinical MRI voxel i.e. with a length scale in the order of mm are required. Such models allow us to explore the links between the geometry of the microvasculature and perfusion and blood pressure measurements, as well as the relationship between flow and metabolism in more detail.

There are various smaller scale models (length scale order 100 μm or less), both cast based and statistical, modelling both human and rat cerebral capillary networks[7–10].

Although useful, these models are too small to provide a direct one-to-one comparison to clinical imaging voxel data. Most of the large-scale models (order mm length scale) that are available in the literature are based on animal models – and most of these are cast based models – due to the relative ease of imaging the microvasculature in animal models to a higher resolution than in the human microvasculature[11–14] – although more recently much progress has been made in acquiring these networks accurately[13], it can still be a labour intensive and expensive process. However, the link between these animal microvasculatures and the human microvasculature has not yet been quantified. For example, rat brains have more penetrating venules than penetrating arterioles in the cortex, which is opposite to the situation in human brains[15,16]. As well as this, these animal models are based on casts which, although valuable in modelling flow and oxygen transport for that particular network, are specific to that given region. The simulation results are thus restricted to the experimental conditions that they were derived from and strongly dependent upon the choice of boundary conditions. Reichold et al.[17] previously attempted to overcome this by using an 'upscaling' approach for averaged quantities of an artificial 2-dimensional capillary network. This averaged network was then coupled to penetrating vessels in a 2-dimensional grid, demonstrating good agreement between the upscaled model and the non-upscaled model. However, since this was only performed for an artificially generated non-morphological network in 2-dimensions, the simulations did not fully represent the rat cerebrovasculature.

In comparison, large-scale models of the human microvasculature are few, mainly due to the relative scarcity (and difficulty) of obtaining physiological data compared to animal models. Lorthois et al.[18] developed a blood flow model based on available human cerebral data[19]; this discrete cast model was found to rely heavily on the prescribed

boundary conditions, with heterogeneities in blood flow within the network controlled by the vascular architecture. The same cerebral data was also used by Linninger et al.[20] to generate a large-scale model that also modelled the individual vessels of the microvasculature discretely, with the capillary network statistically generated matching physiological data, and the penetrating vessels generated using constrained constructive optimization (CCO). Thus, these penetrating vessels are not directly based on physiological data. Additionally, developing larger models of the vasculature becomes very computationally expensive using discrete models such as these.

To the best of our knowledge, there are currently no models of the human microvasculature that investigate the effects of penetrating vessel occlusions on the perfusion and blood pressure of the human microvascular network. The effects of penetrating vessel occlusions (micro-infarcts) have, however, been investigated in mice[21,22] and rats[23] experimentally. The studies found clear conical regions of cerebral tissue supplied by the penetrating vessels, with robustness to blood flow drops/tissue death deeper in the cortex. This led to penetrating arterioles being labelled as a "bottleneck" in cerebral perfusion[22]. Studies in patients with dementia identified a large number of cortical micro-infarcts with diameters in the order 0.1 – 1 mm[24–27]. However, whether these are predictive of or a cause of dementia is as yet unknown due to the inability of conventional clinical imaging to resolve at the length scale of penetrating vessel diameters. As a result, computational models are required to investigate flow at this scale.

The aim of this paper is thus to generate a multi-scale model of the human microvasculature that is able to predict the effect of a penetrating vessel occlusion on local and global flow and perfusion whilst mitigating the effects of the prescribed boundary

conditions. This model is based on physiological data, combining a homogenized capillary bed[28] with statistically generated penetrating vessels[29], is computationally scalable, and generalizable to any available data set. The mean CBF is calculated through these voxel sized models and validated against experimental data. Pressure and volume averaged velocity are investigated, as well as layered flow within the voxels. This is done for both the healthy vasculature and for the occluded vasculature, with the effects of such occlusions compared to the experimental literature.

2. Materials and Methods

The data used in this paper come from the collateral sulcus in the temporal lobe of the human brain. Thick sections of India-ink injected human brain were scanned using confocal laser microscopy and the network reconstructed[19]. Statistical data were extracted from these networks, delineated into capillary and penetrating vessel data. Full details of the data used can be found in the literature[30,19,31,32].

2.1 Morphometry of the microvasculature

The data detailed above have previously been used to generate statistically accurate models of both the cerebral capillary network[10] and the cerebral penetrating vessels[29] which were morphometrically validated against experimental data. The capillary network was then mathematically homogenized[28] to extract the macro-scale properties of the capillary network and to allow these networks to be scaled up to large volumes computationally efficiently. This allows the capillary network to be characterised as a porous medium where the permeability encapsulates the morphological characteristics of the network. This

permeability is calculated from the morphologically accurate networks described above, as detailed previously[28].

A large-scale model (1 x 1 x 2.5mm) of a clinically sized MRI voxel is generated here by combining the models mentioned above. The depth of the model (2.5mm) runs from the pial surface down to the grey matter/white matter interface[31]. The porous capillary bed is assumed to cover the entire volume with a constant, isotropic permeability tensor as previously calculated[28].

The penetrating vessels start at the pial surface and penetrate into the cortex. Their terminal nodes terminate in the porous capillary bed and act as sources and sinks delivering and removing blood to and from the capillary bed. It is assumed that there are 12 penetrating vessels /mm^2 in the ratio 2:1 arterioles-to-venules, as found morphologically[30,33]. As the precise spacing of these vessels is uncertain, and this model is statistical, the 1 mm^2 area is split into 4 quadrants, each containing 2 arterioles and 1 venule randomly placed on the pial surface (Fig. 1a).

Two voxel cases are chosen: case 1 with mean arteriole diameters of 20 μm and mean venule diameters of 50 μm; and case 2 with mean arteriole diameters of 40 μm and mean venule diameters of 110 μm. The latter case is chosen to provide a direct comparison to a previous model of the human microvasculature which used mean arteriole diameters of 40 μm and mean venule diameters of 115 μm[20]. As we wish to investigate the effect of penetrating vessel diameter on flow and pressure pre- and post-occlusion in the network, case 1 is then chosen to have arteriolar diameter half that of the latter case to provide a comparison. The depths of the penetrating vessels were assumed to be linearly related to their diameters with larger diameters penetrating deeper (as observed experimentally)[34].

The arteriole depths were centred on a mean 1.25 mm depth for the mean diameter vessel, and the venules similarly on a 1.75 mm depth. A full list of the parameters used in this voxel model is shown in Table 1. 100 simulations were run for each voxel case, and the density of the penetrating vessel network validated against experimental data. It should be noted that all other attributes of the capillary network and penetrating vessels, such as connectivity, length distributions, area ratios, and bifurcation angles, have previously been validated[10,28,29].

[TABLE 1]

2.2 Simulating blood flow through the voxel

2.2.1 Coupled ODE/PDE model of the blood flow

Using homogenization theory it was previously shown that the capillary bed can be modelled as a porous medium using a volume averaged form of Darcy's law[28]:

$$\langle \mathbf{u}_c \rangle = -\mathbf{K} \nabla p_c \tag{1}$$

where $\langle \mathbf{u}_c \rangle$ is the volume averaged capillary velocity, $\mathbf{K}$ is the permeability tensor, and ∇p_c is the pressure gradient across the capillary bed. The permeability tensor has been shown to be isotropic and diagonally dominant indicating that a constant value of permeability can be used. For this region of the brain this value is equal to 4.28×10^{-4} mm^3 s kg^{-1} [28]. Although in other studies in other organs anisotropy has been assumed[35], in this paper the permeability is assumed throughout to be isotropic as previously determined[28]. This equation can be combined with that of mass conservation:

$$\nabla . \langle \mathbf{u}_c \rangle = S \tag{2}$$

to form:

$$\nabla.(\mathbf{K}\nabla p_c) = -S \tag{3}$$

which is Poisson's equation in 3D, that can be solved for capillary bed pressure. The S term is the source/sink term that comes from the terminal arterioles/venules. This couples the capillary and penetrating vessel models.

The Poiseuille flow equation is then used to model the blood through the penetrating vessels:

$$Q = G\Delta P \tag{4}$$

where:

$$G = \frac{\pi r^4}{8\mu(r)L} \tag{5}$$

where ΔP is the pressure drop in the vessel, Q is the flowrate, G is the conductance of the vessel, L is the length of the vessel, r is the radius of the vessel, and $\mu(r)$ is the apparent viscosity of the blood, which is dependent on the radius due to the Fåhræus-Lindqvist effect and the haematocrit[36].The Fåhræus-Lindqvist effect is accounted for here through a correction for in-vivo viscosity taking into account the endothelial surface layer[37]:

$$\mu_{vitro} = \mu_p \left[1 + (\eta_{0.45} - 1)\frac{(1 - H_{ct})^{C_D} - 1}{(1 - 0.45)^{C_D} - 1}\right] \tag{6}$$

$$\eta_{0.45} = 220e^{-1.3D} + 3.2 - 2.44e^{-0.06D^{0.645}} \tag{7}$$

$$C_D = (0.8 + e^{-0.075D})\left(-1 + \frac{1}{1 + 10^{-11}.D^{12}}\right) + \frac{1}{1 + 10^{-11}.D^{12}} \tag{8}$$

$$\mu_{vivo} = \mu_{vitro} \cdot \left(\frac{D}{D_{eff}}\right)^4 \quad (9)$$

where μ_p is the viscosity of blood plasma (1.2 mPa s), μ_{vitro} is the in-vitro blood viscosity, μ_{vivo} is the apparent in-vivo viscosity, and $\eta_{0.45}$ is the relative apparent viscosity of blood for a discharge haematocrit of 0.45. H_{ct} is the discharge haematocrit, set here to be 0.45[20,38]. The diameter of the blood vessel is D (μm) and D_{eff} is the effective diameter of the blood vessel that takes into account the thickness of the endothelial surface layer, as derived using correlations detailed in Pries & Secomb[37].

As flow is conserved at each bifurcation node, the net flow at each node i is equal to zero, except for at the terminal source and sink nodes. Therefore, for each vessel, flow can be modelled as

$$\sum_{i}^{n} (P_i - P_j) G_{ij} = S_i \quad (10)$$

where G_{ij} is the conductance of the vessel linking node i to node j and is zero unless the connectivity is equal to 1. The source term S_i is zero for all bifurcations except for terminal sources and sinks, and at the inlet to the penetrating vessels. At the pial surface the penetrating arterioles were assigned a pressure of 75 mmHg and the penetrating venules a pressure of 15 mmHg leading to a pressure drop across the voxel of 60 mmHg, based on a previously proposed physiological range[39,40]. This Poiseuille flow model (Eq.10) for the bifurcating trees is then coupled to the discretized form of Eq.3 through the source/sink terms S_i. This coupled model can be solved using a linear solver.

A finite volume discretization is used for Eq.3 with volume sources representing the terminal arterioles and venules. The finite volumes have dimensions of 50 x 50 x 50 $(\mu m)^3$ as this was found to give a good balance between the distribution of sources and sinks within the model and the speed of solution. The coupled model (Eq.3, Eq.10) is solved yielding the nodal pressures in the network from which the Darcy velocity can be found using the discrete form of Eq.1.

2.2.2 Boundary conditions

The results of blood flow simulations in cast models have previously been shown to have a very strong dependence on the boundary conditions[14,18]. However, this issue is mitigated here due to the homogenization of the capillary network. The capillary network is assumed to be periodic, a reasonable assumption due to the randomness of the network[41], in the homogenization procedure, allowing the permeability to be calculated. The value of permeability is, as a result, independent of the pressure gradient. Therefore, the 4 sides of the voxel perpendicular to the pial surface are also given periodic boundary conditions. The pial surface of the voxel is given a no-flow boundary condition, as is the grey matter/white matter interface at the bottom of the voxel. These were considered appropriate boundary conditions as no blood vessels can penetrate beyond the pial surface, and the white matter is much less vascularized than the grey matter[34].

To reduce further the effects of the boundary conditions, the voxel is repeated 4 times to form a larger 2 x 2 x 2.5mm voxel (repeating the voxel being mathematically acceptable due to the periodic boundary conditions). A region of interest is then extracted from this enlarged voxel; a cuboid removed from the centre of size 1 x 1 x 2.5mm (see Fig. 1b). This central region is the one used for analysis.

2.3 Occlusion of a penetrating vessel

The effects of occluding one penetrating vessel in the rat cortex have previously been studied experimentally[21–23]. The model proposed here can also easily be used to study occlusions of penetrating vessels in the human microvasculature. This allows us to determine how much of what can be seen post-occlusion is due to the topological or passive effects of certain regions losing flow, and how much can be better explained using an active response model (which we do not model here). The comparison between experimental penetrating occlusions and this model will thus be discussed in more detail later.

The method of occlusion used here involved identifying the nearest arteriole to the centre of the larger (2 x 2 x 2.5mm) voxel. The region of interest (a cuboid with dimensions 1 x 1 x 2.5mm) is then centred over this penetrating arteriole. The blood flow simulation is run twice for this region: once for the healthy vasculature, and once for when the central arteriole is occluded (the upper portion of the arteriole trunk is occluded so that there is no flow downstream). The difference in the solution between the healthy vasculature and occluded vasculature is taken and this difference is averaged over 100 simulations to observe the averaged effect of a penetrating vessel occlusion on blood pressure and velocity. This same method is used to occlude penetrating venules.

3. Results

3.1 Morphometric validation

One hundred simulations were run to generate statistically accurate voxels of the penetrating vessels; this was done for both voxel cases. The densities of the vessel networks were 674 ± 43, and 659 ± 45 /mm^3, matching morphological densities[30]. The arterioles and

venules also matched their respective morphological densities separately (281 /mm^3 and 385 /mm^3). One example of a statistically generated voxel is given in Fig. 1c.

[FIGURE 1]

3.2 Cerebral blood flow

The CBF is calculated for each voxel by summing the flow leaving the terminal arterioles within the region of interest. This led to a CBF of 39.4 ± 13.9 mL min^{-1} 100g^{-1} for the case 1 voxels (20 µm arterioles; 50 µm venules), and a CBF of 93.75 ± 69.7 mL min^{-1} 100g^{-1} for the case 2 voxels (40 µm arterioles; 110 µm venules), indicating, as expected, a strong influence of the penetrating vessel diameters on CBF. It is highly likely that such large diameter arterioles supply a volume of tissue larger than the voxel considered[38]. The model developed by Linninger et al.[20] had a CBF of 64 mL min^{-1} 100g^{-1}. This lower value of CBF is to be expected, however, due to the lower surface density of the penetrating vessels used (5.33 /mm^2 average in comparison to the 12 /mm^2 used in this paper).

Post-occlusion, the CBF drops across all voxel simulations (see Fig. 2). However, somewhat surprisingly, many of the voxel simulations seem highly robust to the occlusion of a penetrating arteriole, with CBF values dropping by only -7.5% ± 6.3% of the mean CBF value for the case 1 voxels, and -8.2% ± 11.9% for the case 2 voxels (with 60% of the voxels having a CBF drop of less than 5%). These relatively modest average drops in CBF indicate that a single occlusion has only a small effect, one that would be challenging to observe with the resolution of current CBF perfusion imaging. A Wilcoxon signed rank test was run for both size configurations determining that there is a statistically significant drop in flow post-occlusion. However, when comparing the mean drop across both cases, it is found not to be statistically significant (p=0.165).

In order to determine whether there were any boundary effects from the choice of penetrating arteriole to occlude, the distance from the centre of the large cuboid (2 x 2 x2.5 mm) to the position of the chosen penetrating arteriole is plotted against drop in CBF post occlusion (Supplementary Material 2, S.2.6 and S.2.12). No boundary effects were discovered. As well as this, in order to determine what characteristic of the occluded tree most affected the drop in CBF, various properties such as tree volume, penetrating vessel radius, and total tree length were plotted against drops in CBF (Supplementary Material 2, S.2.1 – S.2.12). It was found that whilst the density of the tree, and the number of terminal nodes had little effect, the volume of the tree (along with the total length and penetrating vessel radius) had the largest effects on drops in CBF as has been previously documented[23,29].

[FIGURE 2]

3.3 Pressure and velocity in the healthy vasculature

The averaged pressure and velocity maps of the region of interest (the central section in Fig. 1b) are shown in Fig. 3 for both case 1 and case 2. These show 3D maps of pressure and velocity averaged over the 100 voxels for each configuration. It should be noted that the velocity values quoted here are the volume averaged total velocities (the Darcy velocity) of the capillary network. Depending on the volume fraction of the vasculature in the voxel, this leads to an average velocity in the capillaries in the order of 0.1 – 1 mm s^{-1}, similar to values found experimentally[23,42–44]. Additionally, if the volume averaged velocity is multiplied by the discretized area, we obtain a Darcy flux across the case 1 voxel of 1 – 15 pL s^{-1} and 1 – 18 pL s^{-1} across the case 2 voxel, which compares very favourably to the observed fluxes

calculated for the deep microvessels (with diameters < 10 μm) in rat cortex of 1 – 50 pL s^{-1} [23].

[FIGURE 3]

The first thing to note from these figures is the clearly planar nature of both the pressure and velocity. There appear to be layers of relatively constant pressure and velocity with predominantly a depth-wise gradient. This layering, or shunting, of flow is also seen experimentally[21] and in simulations on casts[12]. What is particularly interesting to note is that the capillary network has been assumed here to be homogenous and isotropic (encapsulated in the constant $\mathbf{K}$ tensor). This indicates that this layered flow within the cortex is a function of the geometry of the penetrating vessels rather than that of the capillary network, with preferential movement of blood flow between the terminal arterioles and terminal venules. This further supports the idea that the capillary bed can be treated as a porous, homogenous, isotropic medium with a given value of permeability. The planar nature of the blood flow can further be seen in Fig. 4 where planar and depth-wise velocity are plotted for the case 1 averaged voxel (the case 2 voxel results being similar). The planar velocity is defined as $\sqrt{u_x^2 + u_y^2}$, where u_x and u_y are the velocities in the x and y directions respectively. The depth-wise velocity is defined as the absolute value of the z-direction velocity. Blood flow is approximately twice as large in the planar direction compared to depth-wise, further supporting the validity of layer specific analysis.

[FIGURE 4]

It can also be seen (Fig. 3c) that larger diameter vessels (as found in the case 2 voxel) impose a much larger pressure gradient over the depth of the voxel – from the pial surface

to the white/grey matter interface – than the smaller diameter vessels (as found in the case 1 voxel). However, despite the increased pressure gradient, we do not see this gradient in the velocity profiles. There thus appears to be a clear decoupling of the pressure gradient and flow within the voxels due to the terminal penetrating vessel nodes acting as sources and sinks within the capillary bed. In other words, the flow is driven by the geometry of the penetrating vessels – the flow is not predominantly pressure gradient driven. Figures S.3.1 and S.3.2 (Supplementary Material 3) also display the terminal node distribution with depth, along with the averaged planar velocity with depth. From these figures, it is clear there is a coupling between the terminal node density and planar velocity.

The mean capillary bed pressure is 38 mmHg for the case 1 voxel, and 43 mmHg for the case 2 voxel. This is consistent with experimental values in the cat mesentery of 35 – 45 mmHg[45], and with models with capillary bed pressures of 30 mmHg[18] and 35 – 40 mmHg[46].

3.4 Effects of occlusion on blood pressure

We next plot the effects of a central arteriole occlusion on blood pressure in Figs. 5 and 6 for the case 1 and case 2 voxels respectively. What is immediately apparent is the central region of reduced blood pressure, with only a small decrease in blood pressure outside this region. As well as this, the central region of reduced blood pressure forms a conical shape, with the area of the region getting smaller with depth until the deep layers exhibit very little pressure drop. This is seen in both the smaller (case 1) and larger (case 2) vessel diameters. This region of reduced blood pressure shows very good agreement with the region of hypoxia post-occlusion that has been identified experimentally in rats[23]: although what was being measured experimentally was the region of tissue hypoxia and necrotic cells, it is shown here that this also overlaps with a region of substantially reduced blood pressure.

[FIGURE 5]

The radius of the blood pressure drop is approximately 250 – 300 μm for the case 1 vessels and between 350 and 450 μm for the (larger) case 2 vessels at their maximum (Fig. 5c, Fig. 6c). Again, this shows good agreement with the experimentally measured region of tissue hypoxia observed post penetrating vessel occlusion of 230 – 250 μm[23] and the region of observed flow drop of 350 μm[22]. Therefore, there appears to be a clear relationship between regions of cell death and regions of reduced blood pressure. Also of interest is the volume of tissue where there is a blood pressure drop. Both the case 1 and case 2 configurations have similar penetrating depths for the blood pressure drop, but the lateral area affected by the occlusion is greater for the case 2 vessels (Fig. 5d, Fig. 6d). This has been shown experimentally by Shih et al., where they also find that occluding larger – hence larger flux – penetrating vessels leads to larger micro-infarcts[23]. It also points towards the robustness of the deep microvasculature in the cortex, a characteristic demonstrated in macaque cerebral tissue[38]. It should be noted that although our model assumes a homogenous, isotropic capillary network, it does again reproduce results found experimentally, seeming to indicate the validity of assuming a homogenous, isotropic capillary network in the grey matter.

[FIGURE 6]

Despite the apparent collateral compensation deeper in the cortex, it should also be noted that the topology of the penetrating vessels strongly affects the local blood pressure, with the occlusion of these vessels causing large drops in blood pressure in the surrounding tissue. This has also been observed in mouse and macaque microvasculatures[14,21]. This

provides further support for the idea proposed by Nishimura et al. that the penetrating vessels are “the bottleneck of perfusion”[22].

3.5 Effects of occlusion on blood velocity

We next plot the effects of an arteriole occlusion on total volume averaged velocity in Figs. 7 and 8 for the case 1 and case 2 voxel configurations respectively. There is clearly a central region of reduced flow, matching the blood pressure drop, but the drop in flow is less spatially confined than the drop in pressure. The drop in flow affects a larger volume of tissue, spreading out further and deeper than the drop in blood pressure. The micro-infarct volume dependence on vessel diameter is again observed, with the larger case 2 vessels having larger regions of flow drop. This difference between the pressure and flow drops again indicates a decoupling of the pressure and flow within the voxel due to the topology of the penetrating vessels – with the flow being driven by the geometry of the terminal vessels more than the voxel-scale pressure gradient.

[FIGURE 7]

The spatial region of flow drop has a clear central core, but spreads through a large region of the voxel (with the case 2 vessels spreading through most of the voxel). This contrasts with the red blood cell (RBC) velocities measured by Nishimura et al. who found that preservation of average flow emerges at a radius of 350 μm away from the occluded penetrating vessel[22]. One potential reason for this discrepancy might be accounted for by the active regulation of the capillary network and neighbouring penetrating vessels, through pericyte contraction and neurotransmitter release, leading to increased perfusion in that region compensating for the widespread drop seen here. It should be noted again that the

model presented in this paper is passive and thus cannot account for either the local or the global regulation of CBF.

It can also be seen that there are small regions/vessels that increase in flow post-occlusion, despite this model being passive. This was also observed in the rat cortex post-occlusion of a penetrating arteriole[22], where a large variability of flow was observed, with both increases and decreases in flow in vessels surrounding the occlusion This large variability in flow is also observed in this model from one voxel simulation to the next. Due to the finite number of voxel simulations, it is thus very likely that this large variability will manifest itself in small regions of increased flow. However, further experiments and more simulations will be required to determine whether this is a robust phenomenon or a result of statistical variability (even with our 100 networks).

[FIGURE 8]

3.6 One-dimensional depth profiles

Based on the planarity shown earlier, it is possible now to look at depth profiles of both the pressure and total velocity. These are shown in Fig. 9, where each layer is 100 μm thick averaged across the plane of the voxel. The pressure and velocity are again found to be decoupled for both the healthy and occluded vasculature due to the geometry of the penetrating vessels. As well as this, despite the larger vessels in the case 2 voxels, and the larger pressure gradient, the planar averaged velocity is similar to the planar averaged velocity in the case 1 voxels. This suggests that the flow in the voxel is predominantly set by the pressure boundary conditions rather than the penetrating vessel diameters. The difference between the healthy and occluded vasculature pressure and velocity distributions is minimal. This means that the effects of a penetrating vessel occlusion are

predominantly local and cannot be seen when averaged over a planar area, as much of the area will not be affected. This is relevant to imaging measurements of CBF as this indicates that penetrating vessel occlusions will be very difficult to observe, due to the minimal effects that they have on averaged flow quantities.

These 1-dimensional distributions were also plotted over a smaller region of interest – 0.5 x 0.5 x 2.5 mm – centred around the penetrating arteriole. The corresponding plots can be found in Supplementary Material 4, S.4.2. Even averaged over this smaller voxel size, the differences in occluded and healthy vasculatures were minimal across both cases.

[FIGURE 9]

3.7 Venous Occlusions

All of the above analysis was also run for penetrating venule occlusions, and the results can be found in Supplementary Material 1. The results are similar to those for the arterioles, with conical pressure change regions, except that when occluding the venule there is a conical pressure increase as opposed to a decrease. The drops in flow however are still diffuse across the voxel. As the venules are larger in size (mean of 50 μm for case 1 and 110 μm for case 2) the drops in CBF in the voxels are larger (case 1: -13.9 ± 10.0% case 2: -19.7 ± 20.3%), with 50% of voxels having a CBF drop of less than 10%. A Wilcoxon signed-rank test was used to determine that there is a statistically significant difference in the CBF drops between occluding an arteriole and occluding a venule at each case.

This indicates that a penetrating venule occlusion is more likely to be detectable than a penetrating arteriole due to the size in flow drop. These results correlate well with those in Shih et al. who also occluded penetrating venules and found that they “generated a microinfarction with notable similarity to that caused by occlusion of a penetrating

arteriole”[23]. As well as this, larger volume, and hence larger flux, penetrating vessels also led to larger volumes of infarction, which again has been observed here with the occlusion of the larger volume penetrating venules. Vessel dilation in upstream capillaries has also been observed experimentally after an occlusion of a penetrating venule[47], however this was not observed in this model due to the lack of a modelled active response.

4. Discussion

The effects of the human microvasculature topology on macro-scale CBF, blood pressure and velocity remain relatively poorly understood. In particular, little is known about the effects of penetrating vessel occlusions in the human microvasculature on pressure and CBF due to the inability of conventional imaging techniques to resolve these small-scale vessels. As a result, we have developed a multi-scale model of the human microvasculature in this paper to analyse the flow properties in voxel sized models for both the healthy and occluded microvasculature. This model was validated by calculating the average CBF for voxels where the arteriolar diameters are 20 µm average (39.4 mL min^{-1} $100g^{-1}$) and 40 µm average (93.75 mL min^{-1} $100g^{-1}$) indicating the very large effect that penetrating vessel diameter has on CBF - an important effect for autoregulation and neurovascular coupling. The range of velocities and fluxes in the capillary network was also found to be between 0.1 – 1 mm s^{-1} and 1 – 18 pL s^{-1} which show good agreement with experimental data[23,42–44].

One of the differences between this model and other large-scale models of the cerebral microvasculature is the treatment of the capillary bed as one homogenous, isotropic, porous medium, characterised by a single value of permeability. Reichold et al.[17] also previously demonstrated the efficacy of this method on an artificial 2-dimensional model of the rat vasculature. In contrast, other models, whether statistical or cast

reconstructions, model capillaries individually[12,18,20,21]. From these models, it has been shown that RBC flow tends to be layered, with shunting of flow between penetrating arterioles and venules terminating at the same depth. This layering is also observed in this model, with very clear planar regions of velocity and pressure, indicating that the layering and shunting of flow is a direct result of the geometry of the penetrating vessels as opposed to the capillary network topology. It also suggests that modelling the capillary network as homogenous and isotropic is a valid assumption, opening up the possibility of further large-scale modelling of the human cerebral microvasculature. However, it should be noted that the simplified modelling approach presented in this paper cannot produce the same level of detail as a cast-based anatomical model, and as such should be used in tandem with such anatomical models, being informed by them as well as using them for validation.

One benefit that a model such as this has is its ability to provide greater detail than a standard MRI voxel, allowing us to observe sub-voxel level detail, whilst also being able to average the flow properties for comparison with conventional imaging voxels. This is seen with the observation that flow and pressure are decoupled within the voxel – with flow preferentially travelling in the planar direction despite a depth-wise pressure gradient. This is due, again, to the geometry of the penetrating arterioles and venules, particularly their terminal vessels that act as sources and sinks within the capillary bed (Supplementary Material 3).

Another benefit of the model presented here is the ability to simulate penetrating vessel occlusions, and to observe how such occlusions affect the behaviour of the cerebral microvasculature. Post-occlusion of an arteriole the CBF was found to drop on average between 7.7 – 8.2%. Post-occlusion of a venule the CBF was found to drop on

average between 13.9 – 19.7%. The CBF robustness to a (smaller diameter) arteriole occlusion demonstrates that such micro-infarcts will be very difficult to pick up using current clinical MRI perfusion imaging. This agrees with what was previously found by El-Bouri and Payne [29]: i.e. that the topology of the penetrating vessels contributes only a small amount to the CBF variability; the radius on the other hand has a much larger effect on the CBF. This indicates that occluded venules are much more likely to picked up using current clinical MRI techniques. Within the voxel, the difference in pressure between the occluded and healthy vasculature shows clear conical regions of blood pressure drop, which overlie very well with the regions of tissue hypoxia observed post-occlusion in rats[23]. Larger diameter vessels, hence larger flux vessels, exhibited larger volumes of blood pressure drop – again correlating with what is found experimentally[23]. Blood pressure deeper into the grey matter was less affected by the occlusion than that at the surface layers. As few penetrating vessels reach the deepest layers, this is likely to be a topological effect, with the drop in pressure in the voxel being very heavily dependent on the location of the penetrating vessels and their terminal nodes. This backs up the idea that the penetrating vessel is "the bottleneck of perfusion"[22]. The reproduction of these experimental results again demonstrates the validity of assuming a homogenous, isotropic capillary network.

The decoupling in pressure and flow was also observed with the occluded microvasculature. The conical regions of pressure drop were not emulated in perfusion, with perfusion drop being far more diffuse across the voxel. Nishimura et al. found that the RBC velocity returns to baseline beyond a 350 μm radius around the occluded vessel[22]. This is not seen in this model, indicating that there is an active response in the capillary network around the penetrating vessel that restores flow up to this point. However, in the direct

vicinity of the penetrating vessel flow cannot be restored, due to the reliance on that region of tissue on the topology of particular penetrating vessels.

This highlights one of the major limitations of the model which is the lack of an active response. It is currently thought that capillary pericytes actively regulate capillary dilation, with capillary dilation occurring before arteriolar dilation, and contributing up to 84% of the blood flow increase in that region[48]. However, this is a topic of ongoing debate, with other mechanisms proposed as potential pathways in capillary dilation[49–51]. Other potential discrepancies between modelled and experimental findings may also be due to other biological mechanisms that are not modelled, such as the adhesion of leukocytes[52]. Regardless, it seems that the capillary bed plays an active role in the regulation of cerebral blood flow through the pericytes. The model presented here is purely passive and so cannot predict changes in the microvasculature post-occlusion. Therefore, the next step will be to model an active response to see how changes in the microvasculature affect post-clot perfusion and blood pressure, and how much effect the active response has in comparison to the passive response.

This active response will need to be modelled with feedback based on (most likely) a hypoxia model to determine where the response is activated. This would be incorporated via a temporally and spatially varying permeability that would be pre-computed[28] from the simulation of dilating vessels in statistically accurate anatomical models. Although it is thought that dilation of vessels will increase the permeability, the exact relationship between dilation and its effect on permeability is not yet known and this will be the subject of future work. Such simulations of autoregulation on this homogenized model can then be cross-validated against more detailed anatomical models. As well as this, density variations

within the cortex can also be incorporated via a spatially varying permeability straightforwardly. These density variations, which have not been modelled, may account for some of the discrepancy in the flow model and experimental work. As well as this, the spatial pattern of the penetrating arterioles and venules may also have an effect on the modelled results, and hence the flow discrepancies observed, but in the absence of any data on what these patterns are in the human cortex, this remains an unknown quantity.

Beyond these improvements, a variable haematocrit model should be included in future, as currently a constant haematocrit is assumed, although it is likely that this will have only a second order effect[14]. Simulation of this bi-phasic flow can be performed in a similar fashion to that in Gould and Linninger[53] in order to pre-compute the permeability tensor which can then be used in the multi-scale model presented in this paper.

The model can be further validated in future against MRI voxels once an oxygen transport model has been added. Perfusion MRI imaging can also be used to derive experimentally a transit time distribution (TTD), which could be calculated using the model presented here along with an oxygen transport mechanism[54,55]. The TTD could then be calculated across a number of simulated voxels and compared to human data for the same region of brain. Such a model would be valuable in helping us further to observe the layered effects of blood flow, as well as the effects of flow regulation on blood pressure and perfusion post-occlusion. It would also be valuable in comparing oxygen transport in this homogenous capillary bed with oxygen transport in cast based models[13,20]. This will aid in determining whether there is capillary flow homogenization in passive and active states. A further benefit of this model is that it will be able to potentially predict MRI resolutions that will be able to pick up a penetrating vessel occlusion, although the exact method for this

analysis is a subject for future work. Most importantly, however, this model will allow us to draw a clearer link between the 'unseen' microvasculature and MRI scans in future, helping to bridge the 'imaging gap' that currently exists.

Declaration of Conflicting Interests

The authors declare that there is no conflict of interest.

Acknowledgements

W.K. El-Bouri is funded by an EPSRC Doctoral Training Partnership studentship, grant reference EP/M50659X/1

References

1. Bullitt E, Zeng D, Gerig G, et al. Vessel tortuosity and brain tumor malignancy: a blinded study. *Acad Radiol* 2005; 12: 1232–1240.

2. Jain RK. Normalization of tumor vasculature: an emerging concept in antiangiogenic therapy. *Science (80-)* 2005; 307: 58–62.

3. Jellinger KA. The pathology of 'vascular dementia': a critical update. *J Alzheimers Dis* 2008; 14: 107–123.

4. Meyer EP, Ulmann-Schuler A, Staufenbiel M, et al. Altered morphology and 3D architecture of brain vasculature in a mouse model for Alzheimer's disease. *Proc Natl Acad Sci U S A* 2008; 105: 3587–3592.

5. Toledo JB, Arnold SE, Raible K, et al. Contribution of cerebrovascular disease in autopsy confirmed neurodegenerative disease cases in the National Alzheimer's Coordinating Centre. *Brain* 2013; 136: 2697–2706.

6. Mut F, Wright S, Ascoli GA, et al. Morphometric, geographic, and territorial characterization of brain arterial trees. *Int J Numer Method Biomed Eng* 2014; 30: 755–766.

7. Fang Q, Sakadzic S, Ruvinskaya L, et al. Oxygen advection and diffusion in a three-dimensional vascular anatomical network. *Opt Express* 2008; 16: 17530–17541.

8. Safaeian N, David T. A computational model of oxygen transport in the cerebrocapillary levels for normal and pathologic brain function. *J Cereb Blood Flow Metab* 2013; 33: 1633–1641.

9. Secomb TW, Hsu R, Beamer NB, et al. Theoretical simulation of oxygen transport to brain by networks of microvessels: effects of oxygen supply and demand on tissue hypoxia. *Microcirculation* 2000; 7: 237–247.

10. Su SW, Catherall M, Payne S. The influence of network structure on the transport of blood in the human cerebral microvasculature. *Microcirculation* 2012; 19: 175–187.

11. Gagnon L, Sakadžić S, Lesage F, et al. Quantifying the Microvascular Origin of BOLD-fMRI from First

Principles with Two-Photon Microscopy and an Oxygen-Sensitive Nanoprobe. *J Neurosci* 2015; 35: 3663–3675.

12. Schmid F, Tsai PS, Kleinfeld D, et al. Depth-dependent flow and pressure characteristics in cortical microvascular networks. *PLOS Comput Biol* 2017; 13: e1005392.

13. Gould IG, Tsai P, Kleinfeld D, et al. The capillary bed offers the largest hemodynamic resistance to the cortical blood supply. *J Cereb Blood Flow Metab* 2017; 37: 52–68.

14. Guibert R, Fonta C, Plouraboue F. Cerebral blood flow modeling in primate cortex. *J Cereb Blood Flow Metab* 2010; 30: 1860–1873.

15. Blinder P, Shih AY, Rafie C, et al. Topological basis for the robust distribution of blood to rodent neocortex. *Proc Natl Acad Sci* 2010; 107: 12670–12675.

16. Schmid F, Barrett MJP, Jenny P, et al. Vascular density and distribution in neocortex. *Neuroimage*. Epub ahead of print 2017. DOI: http://dx.doi.org/10.1016/j.neuroimage.2017.06.046.

17. Reichold J, Stampanoni M, Lena Keller A, et al. Vascular graph model to simulate the cerebral blood flow in realistic vascular networks. *J Cereb Blood Flow Metab* 2009; 29: 1429–1443.

18. Lorthois S, Cassot F, Lauwers F. Simulation study of brain blood flow regulation by intra-cortical arterioles in an anatomically accurate large human vascular network: Part I: methodology and baseline flow. *Neuroimage* 2011; 54: 1031–1042.

19. Cassot F, Lauwers F, Fouard C, et al. A novel three-dimensional computer-assisted method for a quantitative study of microvascular networks of the human cerebral cortex. *Microcirculation* 2006; 13: 1–18.

20. Linninger AA, Gould IG, Marinnan T, et al. Cerebral Microcirculation and Oxygen Tension in the Human Secondary Cortex. *Ann Biomed Eng* 2013; 41: 2264–2284.

21. Blinder P, Tsai PS, Kaufhold JP, et al. The cortical angiome: an interconnected vascular network with noncolumnar patterns of blood flow. *Nat Neurosci* 2013; 16: 889–897.

22. Nishimura N, Schaffer CB, Friedman B, et al. Penetrating arterioles are a bottleneck in the perfusion of neocortex. *Proc Natl Acad Sci U S A* 2007; 104: 365–370.

23. Shih AY, Blinder P, Tsai PS, et al. The smallest stroke: Occlusion of one penetrating vessel leads to infarction and a cognitive deficit. *Nat Neurosci* 2013; 16: 55–63.

24. Arvanitakis Z, Leurgans SE, Barnes LL, et al. Microinfarct pathology, dementia, and cognitive systems. *Stroke* 2011; 42: 722–727.

25. Jouvent E, Poupon C, Gray F, et al. Intracortical infarcts in small vessel disease: a combined 7-T postmortem MRI and neuropathological case study in cerebral autosomal-dominant arteriopathy with subcortical infarcts and leukoencephalopathy. *Stroke* 2011; 42: e27-30.

26. Kovari E, Gold G, Herrmann FR, et al. Cortical microinfarcts and demyelination affect cognition in cases at high risk for dementia. *Neurology* 2007; 68: 927–931.

27. Vinters H V, Ellis WG, Zarow C, et al. Neuropathologic substrates of ischemic vascular dementia. *J Neuropathol Exp Neurol* 2000; 59: 931–945.

28. El-Bouri WK, Payne SJ. Multi-scale homogenization of blood flow in 3-dimensional human cerebral microvascular networks. *J Theor Biol* 2015; 380: 40–47.

29. El-Bouri WK, Payne SJ. A statistical model of the penetrating arterioles and venules in the human cerebral cortex. *Microcirculation* 2016; 23: 580–590.

30. Cassot F, Lauwers F, Lorthois S, et al. Branching patterns for arterioles and venules of the human cerebral cortex. *Brain Res* 2010; 1313: 62–78.

31. Lauwers F, Cassot F, Lauwers-Cances V, et al. Morphometry of the human cerebral cortex microcirculation: general characteristics and space-related profiles. *Neuroimage* 2008; 39: 936–948.

32. Lorthois S, Lauwers F, Cassot F. Tortuosity and other vessel attributes for arterioles and venules of the human cerebral cortex. *Microvasc Res* 2014; 91: 99–109.

33. Risser L, Plouraboue F, Cloetens P, et al. A 3D-investigation shows that angiogenesis in primate cerebral cortex mainly occurs at capillary level. *Int J Dev Neurosci* 2009; 27: 185–196.

34. Duvernoy HM, Delon S, Vannson JL. Cortical blood vessels of the human brain. *Brain Res Bull* 1981; 7: 519–579.

35. Hyde ER, Cookson AN, Lee J, et al. Multi-scale parameterisation of a myocardial perfusion model using whole-organ arterial networks. *Ann Biomed Eng* 2014; 42: 797–811.

36. Fahraeus R, Lindqvist T. The viscosity of the blood in narrow capillary tubes. *Amer J Physiol* 1931; 96: 562–568.

37. Pries AR, Secomb TW. Microvascular blood viscosity in vivo and the endothelial surface layer. *Am J Physiol Hear Circ Physiol* 2005; 289: H2657-64.

38. Guibert R, Fonta C, Risser L, et al. Coupling and robustness of intra-cortical vascular territories. *Neuroimage* 2012; 62: 408–417.

39. Stromberg DD, Fox JR. Pressures in the pial arterial microcirculation of the cat during changes in systemic arterial blood pressure. *Circ Res* 1972; 31: 229–239.

40. Tamaki K, Heistad DD. Response of cerebral arteries to sympathetic stimulation during acute hypertension. *Hypertension* 1986; 8: 911–917.

41. Auriault JL. Heterogeneous periodic and random media. Are the equivalent macroscopic descriptions similar? *Int J Eng Sci* 2011; 49: 806–808.

42. Stefanovic B, Hutchinson E, Yakovleva V, et al. Functional reactivity of cerebral capillaries. *J Cereb Blood Flow Metab* 2008; 28: 961–972.

43. Kleinfeld D, Mitra PP, Helmchen F, et al. Fluctuations and stimulus-induced changes in blood flow observed in individual capillaries in layers 2 through 4 of rat neocortex. *Proc Natl Acad Sci U S A* 1998; 95: 15741–15746.

44. Gutierrez-Jimenez E, Cai C, Mikkelsen IK, et al. Effect of electrical forepaw stimulation on capillary transit-time heterogeneity (CTH). *J Cereb Blood Flow Metab* 2016; 36: 2072–2086.

45. Lipowsky HH. Microvascular rheology and hemodynamics. *Microcirculation* 2005; 12: 5–15.

46. Boas DA, Jones SR, Devor A, et al. A vascular anatomical network model of the spatio-temporal response to brain activation. *Neuroimage* 2008; 40: 1116–1129.

47. Nguyen J, Nishimura N, Fetcho RN, et al. Occlusion of Cortical Ascending Venules Causes Blood Flow Decreases, Reversals in Flow Direction, and Vessel Dilation in Upstream Capillaries. *J Cereb Blood Flow Metab* 2011; 31: 2243–2254.

48. Hall CN, Reynell C, Gesslein B, et al. Capillary pericytes regulate cerebral blood flow in health and disease. *Nature* 2014; 508: 55–60.

49. Hill RA, Tong L, Yuan P, et al. Regional Blood Flow in the Normal and Ischemic Brain Is Controlled by Arteriolar Smooth Muscle Cell Contractility and Not by Capillary Pericytes. *Neuron* 2015; 87: 95–110.

50. Fernandez-Klett F, Offenhauser N, Dirnagl U, et al. Pericytes in capillaries are contractile in vivo, but arterioles mediate functional hyperemia in the mouse brain. *Proc Natl Acad Sci U S A* 2010; 107: 22290–22295.

51. Fernandez-Klett F, Priller J. Diverse Functions of Pericytes in Cerebral Blood Flow Regulation and Ischemia. *J Cereb Blood Flow Metab* 2015; 35: 883–887.

52. Yilmaz G, Granger DN. CELL ADHESION MOLECULES AND ISCHEMIC STROKE. *Neurol Res* 2008; 30: 783–793.

53. Gould IG, Linninger AA. Hematocrit Distribution and Tissue Oxygenation in Large Microcirculatory Networks. *Microcirculation* 2015; 22: 1–18.

54. Park CS, Payne SJ. A generalized mathematical framework for estimating the residue function for arbitrary vascular networks. *Interface Focus* 2013; 3: 20120078.

55. Park CS, Payne SJ. Modelling the effects of cerebral microvasculature morphology on oxygen transport. *Med Eng Phys* 2016; 38: 41–47.

Tables

Table 1. Values used to model the blood flow through the voxel

Variable	Morphological Values	Model Values
Arteriole Diameter (µm)	15 – 240[34]	Case 1: 20 ± 5
		Case 2: 40 ± 8
Venule Diameter (µm)	20 -125[34]	Case 1: 50 ± 10
		Case 2: 110 ± 16
Arteriole Length (mm)	Up to 2.5[31,34]	Case 1: 1.25 ± 0.31
		Case 2: 1.25 ± 0.25
Venule Length (mm)	Up to 2.5[31,34]	Case 1: 1.75 ± 0.35
		Case 2: 1.75 ± 0.25
Surface Density (/mm^2)	8.44 – 15[33]	12
Arteriole Pial Pressure (mmHg)	65 – 90[39,40]	75
Venule Pial Pressure (mmHg)	15 – 25[39,40]	15
Capillary Bed Permeability (mm^3 s kg^{-1})	N/A	4.28 x 10^{-4} [28]
Voxel Dimensions (Length x Width x Depth) – (mm)	-	1 x 1 x 2.5

Figures

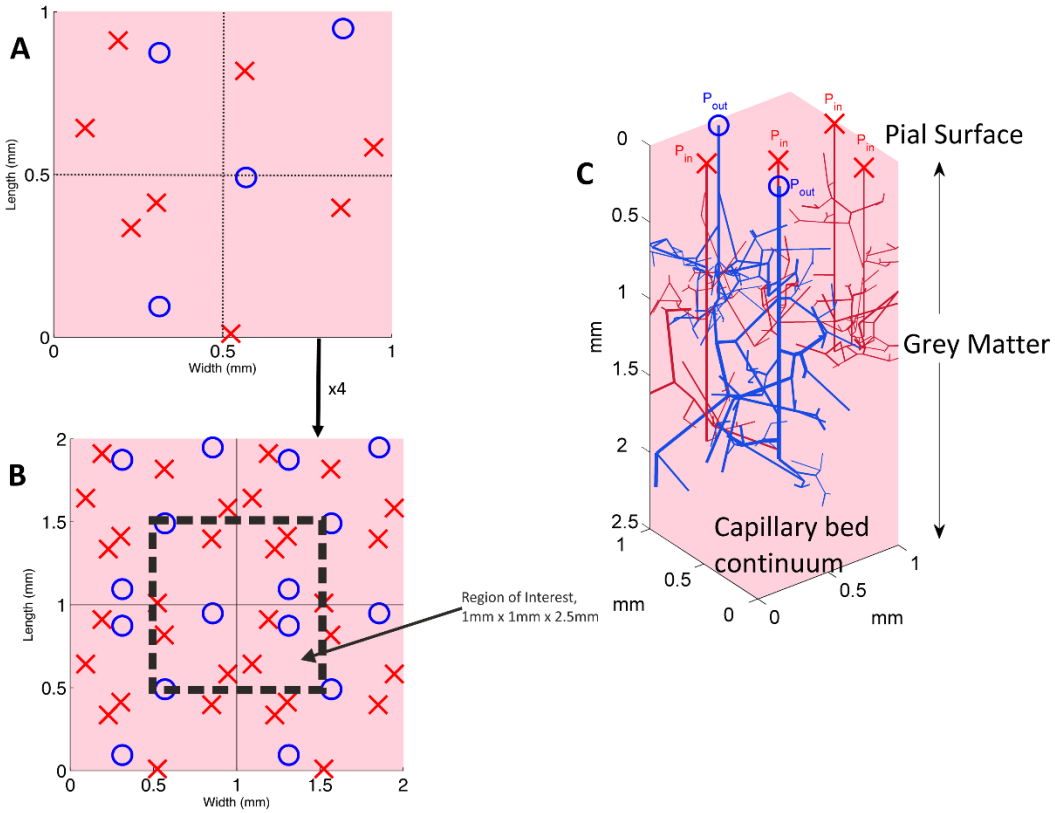

FIG. 1 a) Top down view of a 1 x 1 x 2.5 mm voxel, split into 4 quadrants each containing 2 arterioles and 1 venule. b) The same voxel as in a) repeated 4 times to form a 2 x 2 x 2.5 mm voxel. The region of interest is shown as the black dashed line. c) An example voxel showing half the penetrating vessels for easier viewing. The penetrating vessels enter from the pial surface into the grey matter, coupling to the capillary bed continuum via the terminal vessels.

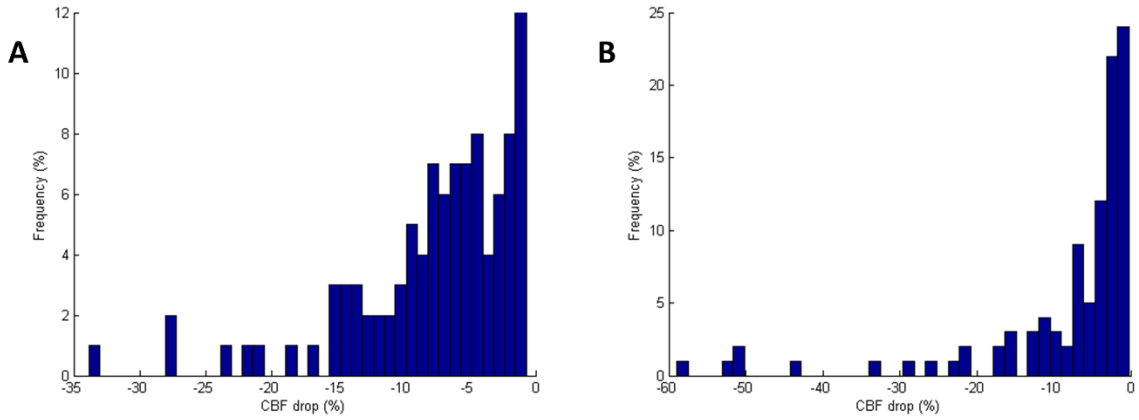

FIG. 2 Histogram of the change in CBF post-occlusion of a central arteriole in every voxel. a) Case 1: 20 – 50 µm vessels; b) Case 2: 40 – 110 µm vessels

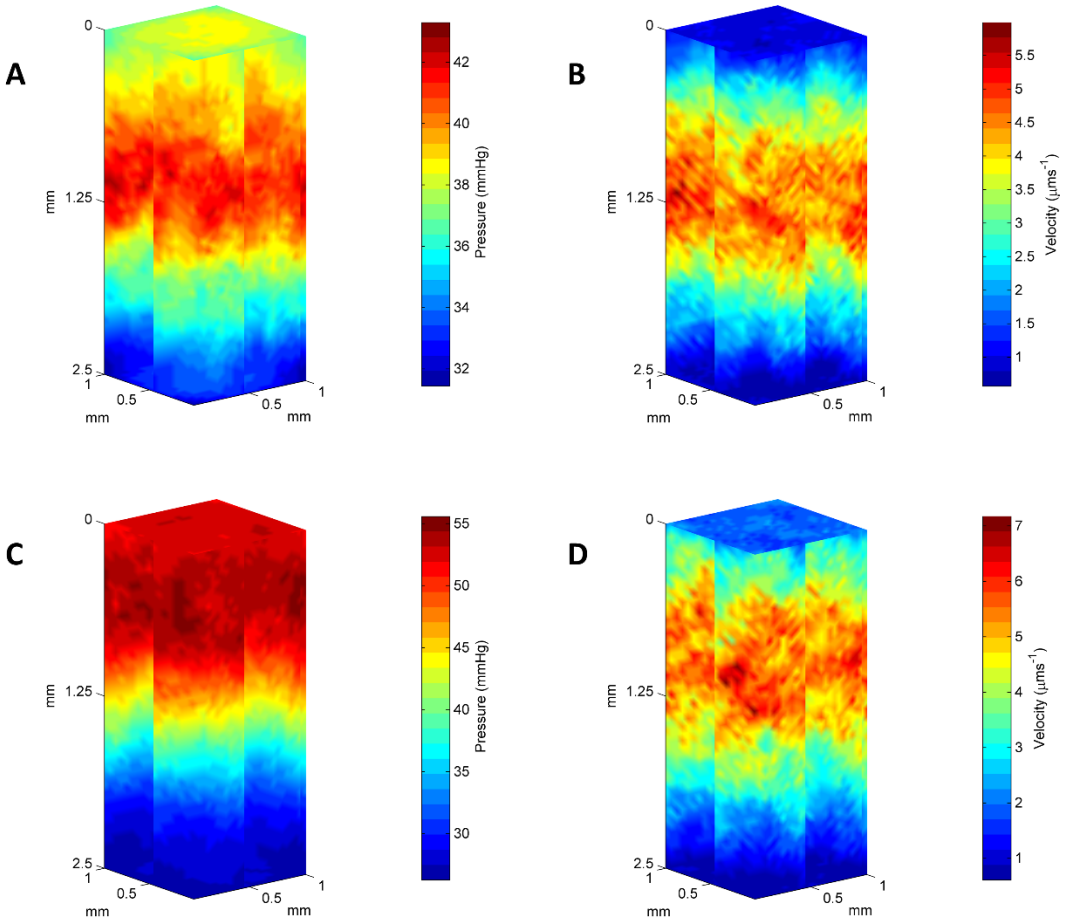

FIG. 3 Pressure and velocity maps for Case 1 (20 – 50 μm) configuration: a) 3D map of pressure in the region of interest; b) 3D map of Darcy velocity in the region of interest. Pressure and velocity maps for Case 2 (40 – 110 μm) configuration: c) 3D map of pressure in the region of interest; d) 3D map of Darcy velocity in the region of interest. It should be noted that pial vessels are not considered, and hence their pressure and flow not plotted, in this analysis. All 3D voxels are plotted with projections in the x = 0.5 and y = 0.5 planes.

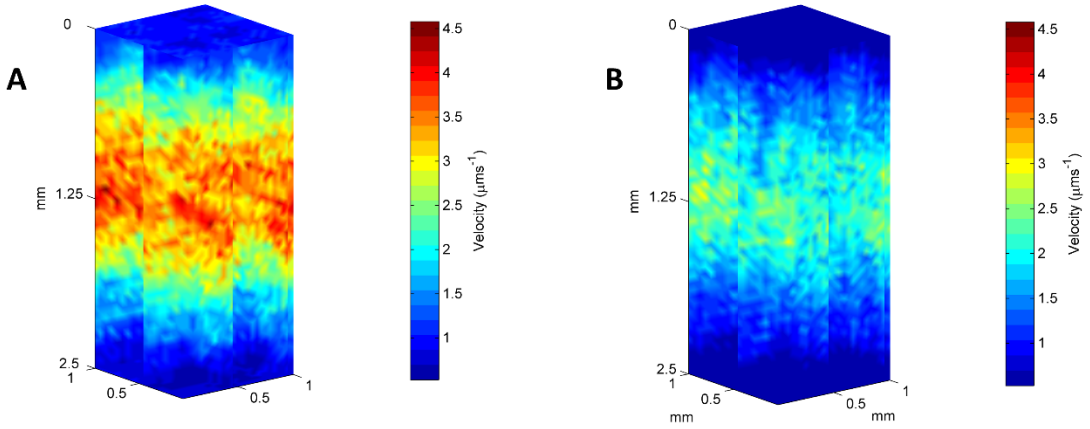

FIG. 4 Case 1 voxel: (a) Planar Darcy velocity; and (b) depth-wise Darcy velocity

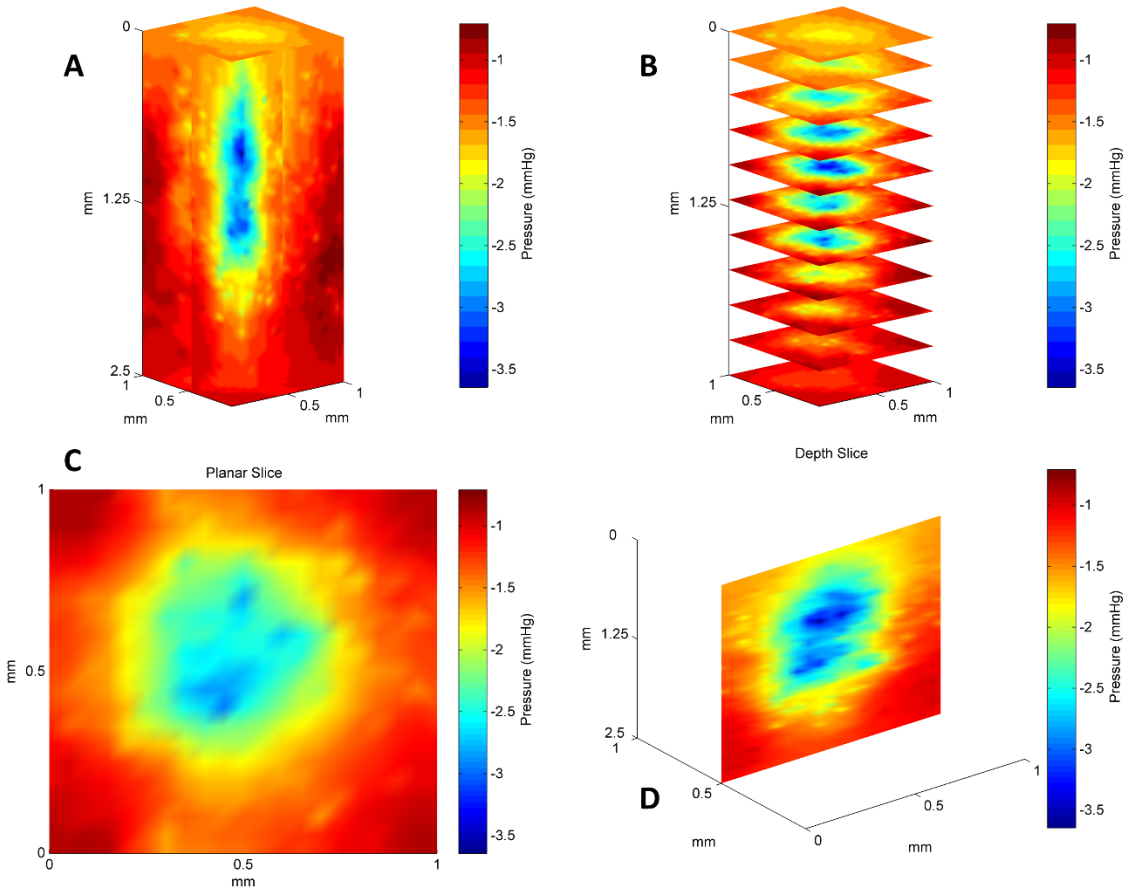

FIG. 5 Pressure difference between the averaged healthy and occluded vasculature for the Case 1 configuration. a) 3D map of pressure difference displaying a clear central region of blood pressure drop. b) Slices of the pressure map taken at 250 µm intervals through the depth of the voxel, clearly displaying the conical nature of the blood pressure drop. c) Planar slice taken 1.25 mm down the voxel showing a circular region of pressure drop, with a radius of around 250 µm. d) Planar slice taken depth-wise through the voxel 0.5 mm along the width of the voxel, again showing the conical nature of the pressure drop.

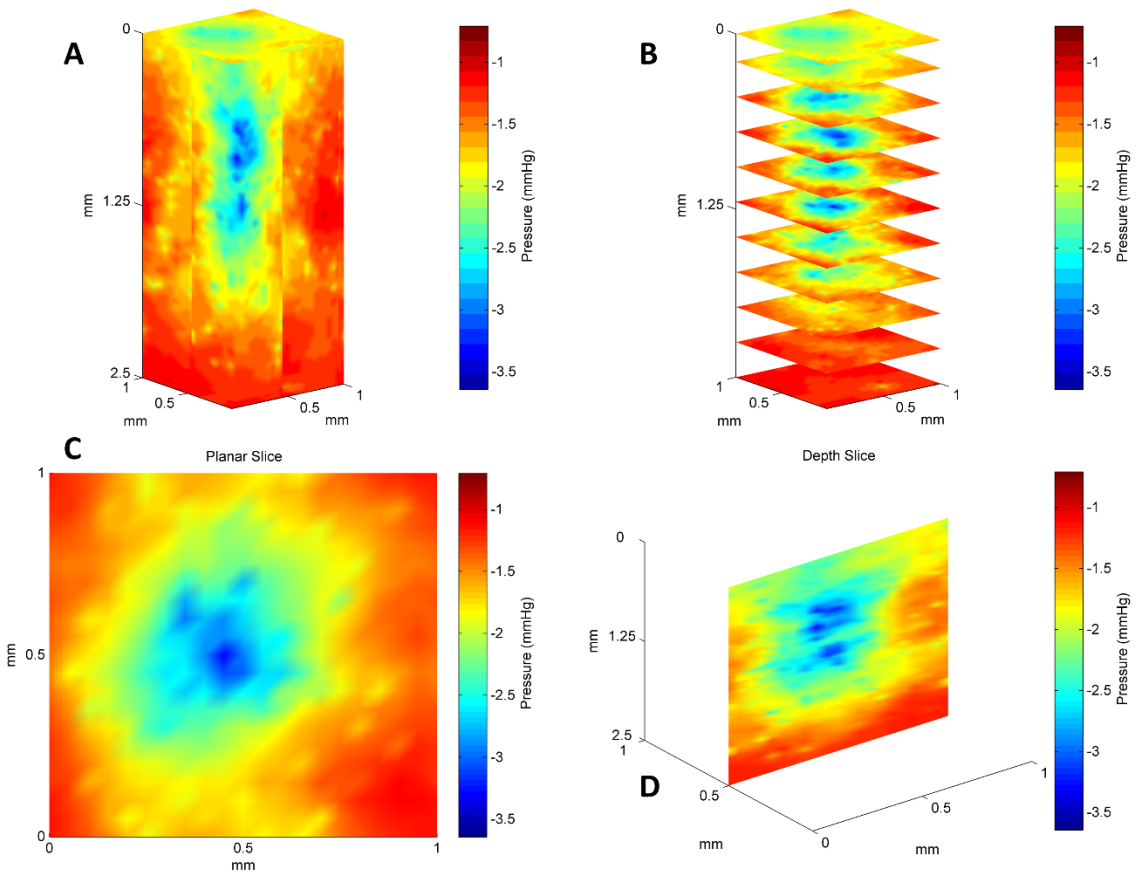

FIG. 6 Pressure difference between the averaged healthy and occluded vasculature for the Case 2 configuration. a) 3D map of pressure difference displaying a clear central region of blood pressure drop. b) Slices of the pressure map taken at 250 µm intervals through the depth of the voxel, clearly displaying the conical nature of the blood pressure drop. c) Planar slice taken 1.25 mm down the voxel showing a circular region of pressure drop, with a radius of around 350 µm. d) Planar slice taken depth-wise through the voxel 0.5 mm along the width of the voxel, again showing the conical nature of the pressure drop.

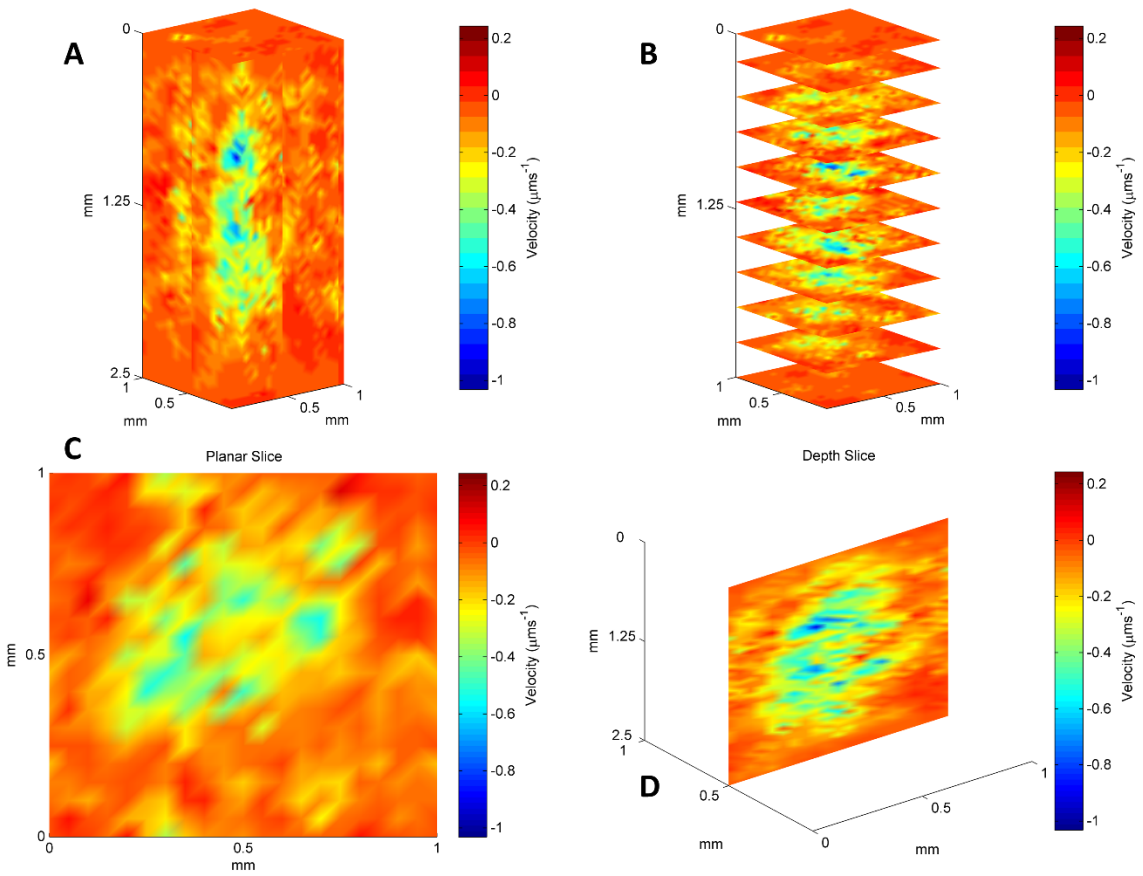

FIG. 7 Volume averaged velocity difference between the averaged healthy and occluded vasculature for the Case 1 configuration. a) 3D map of velocity difference displaying a central region of blood velocity drop. b) Slices of the velocity map taken at 250 μm intervals through the depth of the voxel. c) Planar slice taken 1.25 mm down the voxel. d) A planar slice taken depth-wise through the voxel 0.5 mm along the width of the voxel, showing an expansive region of blood velocity drop.

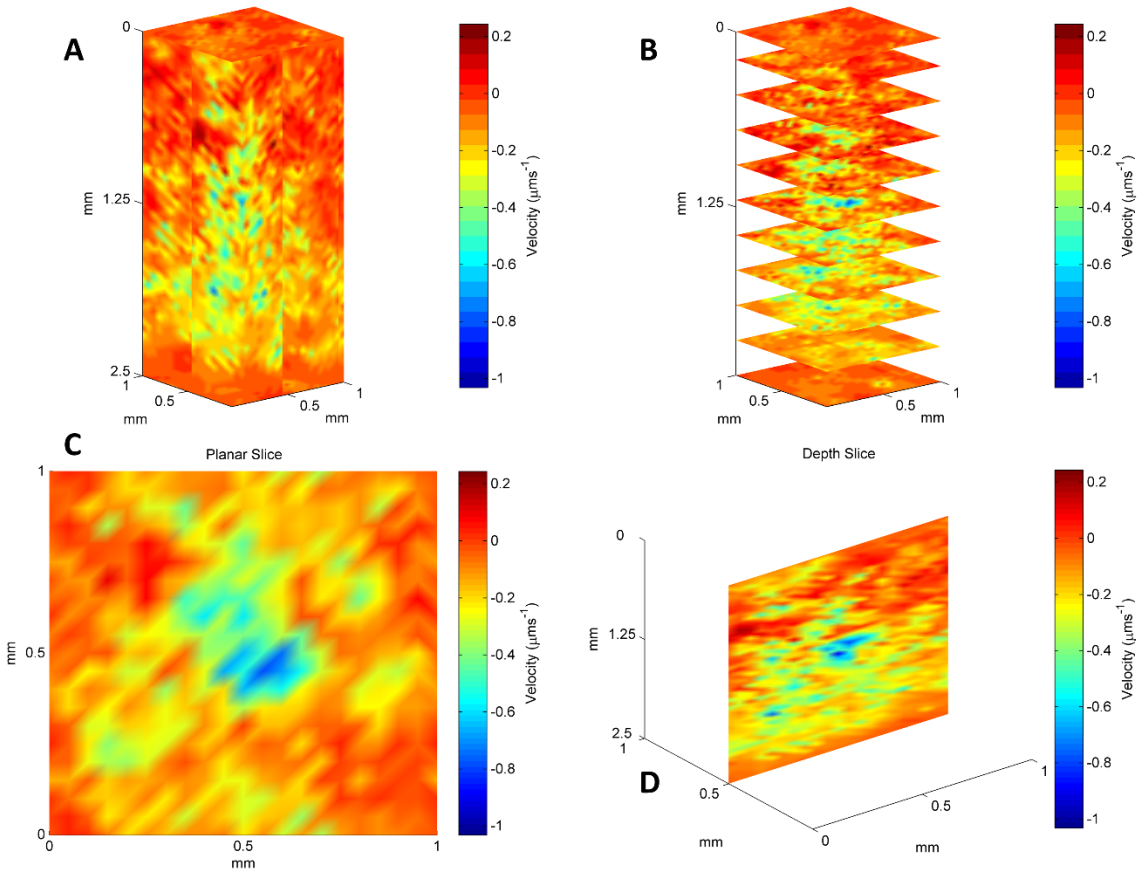

FIG. 8 Volume averaged velocity difference between the averaged healthy and occluded vasculature for the Case 2 configuration. a) 3D map of velocity difference displaying a more diffuse region of blood velocity drop. b) Slices of the velocity map taken at 250 μm intervals through the depth of the voxel. c) Planar slice taken 1.25 mm down the voxel. d) A planar slice taken depth-wise through the voxel 0.5 mm along the width of the voxel, showing an expansive region of blood velocity drop.

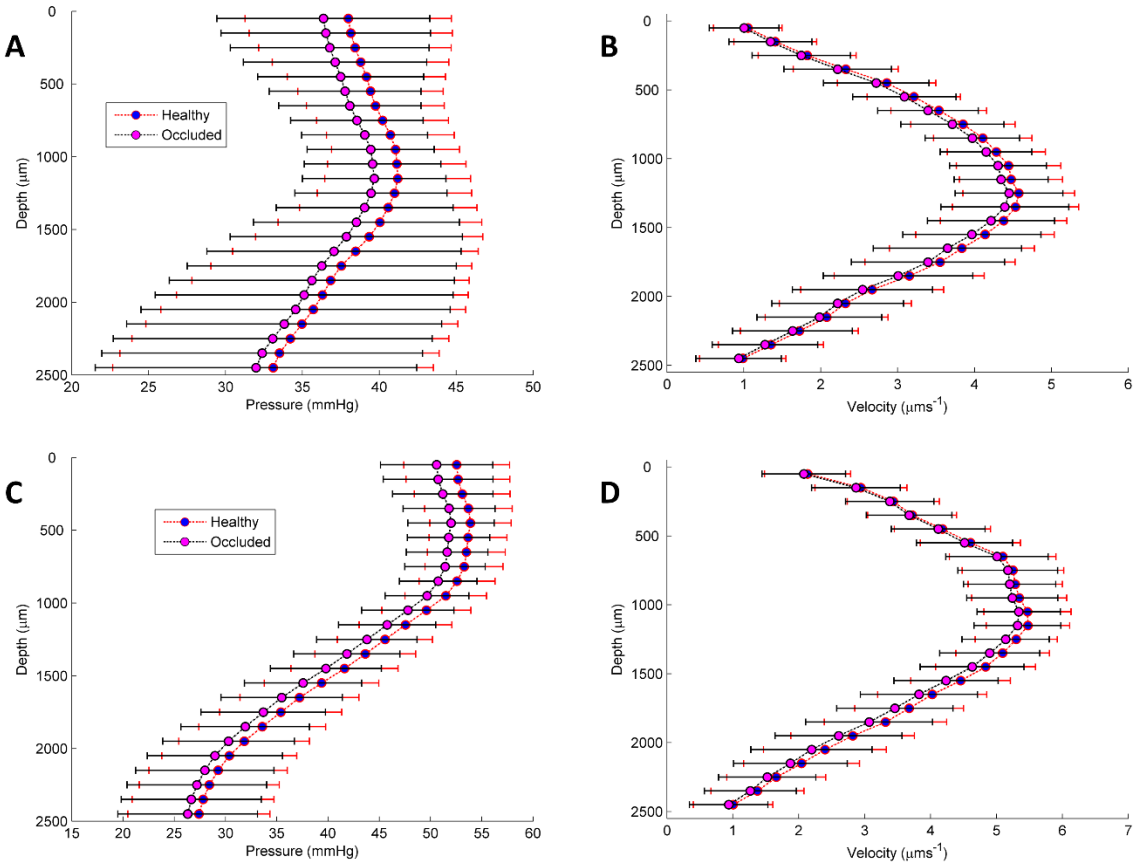

FIG. 9 a,b) 1-D planar averaged depth profiles of pressure and total velocity for the case 1 configuration. c,d) 1-D planar averaged depth profiles of pressure and total velocity for the case 2 configuration. Blue solid circles – Healthy vasculature; Magenta solid circles – Occluded vasculature.